


Visible-band polarization-entangled photon source by quantum frequency transduction

Ren-Hui Chen,^{1,2,*} Su-Jian Niu,^{1,2} Zheng Ge,^{1,2} Zhao-Qi-Zhi Han^{ⓧ,1,2}, Xiao-Hua Wang,^{1,2}
Hai Jiang^{ⓧ,3,†}, Zhi-Yuan Zhou^{ⓧ,1,2,‡} and Bao-Sen Shi^{1,2,§}

¹*CAS Key Laboratory of Quantum Information, University of Science and Technology of China, Hefei, Anhui 230026, China*

²*Synergetic Innovation Center of Quantum Information & Quantum Physics, University of Science and Technology of China, Hefei, Anhui 230026, China*

³*National Astronomical Observatories, Chinese Academy of Sciences, 100101, China*

 (Received 21 November 2023; revised 6 May 2024; accepted 14 June 2024; published 9 July 2024)

Visible-band polarization-entangled photon sources (VBPEPSs) are preferred in quantum microscopy, imaging, and light-matter interactions with solid-state quantum memories, N-*V* centers, and trapped ions. They can be generated directly via spontaneous parametric down-conversion. However, that requires a high-power deep-ultraviolet pump laser. Additionally, the required ultraviolet-band nonlinear crystal is inefficient compared to periodically poled potassium titanyl phosphate or periodically poled lithium niobate crystals. The quantum frequency transduction of a near-infrared polarization-entangled photon source (NIPEPS) provides an effective way to overcome the drawbacks of direct generation. We demonstrate 634-nm VBPEPS generation via polarization-independent frequency transduction of 1080-nm NIPEPS. High-quality entanglement in the visible band is verified via two-photon polarization interference, Bell-inequality, and quantum-state tomography. This method could be applied to other visible wavelengths or be extended to the ultraviolet, which is difficult to generate directly. It has promising applications in quantum imaging, networks, and spectroscopy.

DOI: [10.1103/PhysRevApplied.22.014020](https://doi.org/10.1103/PhysRevApplied.22.014020)

I. INTRODUCTION

Quantum communications, computations, and sensors are indispensable building blocks for future quantum network applications [1,2]. These fundamental building blocks should be linked with entangled photon-pair sources. The preferred physical quantum systems for constructing a quantum network often operate at different wavelengths. For example, preferred wavelengths for long-distance communication are in the 1550-nm telecom band, while the visible band is used for materials coupling, such as atomic ensembles, trapped ions, rare-earth ion-doped solid-state crystals, and N-*V* centers [3–6]. Therefore, it is necessary to prepare an entangled photon source with a specific spectrum for certain quantum network applications.

Polarization-entangled photon sources (PEPSs) have been extensively studied for decades because of the ease in generation, control, and measurement. PEPSs can

be directly produced via spontaneous parametric down-conversion (SPDC) [7] or spontaneous four-wave mixing [8–10]. The Sagnac-loop interferometer and crossed crystals are the most commonly used configurations for generating PEPS [11,12]. Although they have been widely used for the generation of near-infrared polarization-entangled photon sources (NIPEPSs) [13], it would be difficult to efficiently extend these configurations to short-wave visible-band PEPS (VBPEPS) or ultraviolet PEPS for the following reasons. (i) Direct generation of PEPS at specific wavelengths via SPDC requires a shorter wavelength of pump light. Therefore, generating short-wave VBPEPS or ultraviolet PEPS requires the crystal to operate in the deep-ultraviolet band. The operation of nonlinear crystals in these bands such as LBO, BBO is inefficient when the effective nonlinear coefficients are low and crystals' length is short [14], thus requires high-power deep-ultraviolet or vacuum-ultraviolet pump lasers [15], which are not easily available [16]. (ii) High-quality deep-ultraviolet or vacuum-ultraviolet optical elements such as waveplates and filters are also not readily available. In addition, VBPEPS is preferred for quantum optical microscopy, imaging, quantum spectroscopy, and light-matter interactions with rare-earth ion-doped solid-state crystals, N-*V* centers, and trapped ions. Therefore, it is necessary to

* Contact author: chenrenhui@mail.ustc.edu.cn

† Contact author: jhai@nao.cas.cn

‡ Contact author: zyzhouphy@ustc.edu.cn

§ Contact author: drshi@ustc.edu.cn

develop high-quality VBPEPS, and quantum frequency transduction (QFT) is a viable solution to the issues faced by direct generation methods. The quantum nature of a photon can be preserved by QFT, even after it has been converted to a different wavelength [17]. QFT based on three-wave mixing typically does not preserve the polarization of the input photon because of phase matching. Several configurations for polarization-independent QFT (PIQFT) have been developed to meet this challenge [18–20]. A high-efficiency, single-bit PIQFT has been demonstrated with a waveguide crystal in a Sagnac-loop configuration, which converts 842-nm photons to the 1550-nm band [21]. With an improved PIQFT performance, entanglement of two atomic ensemble nodes separated by 33 km was realized [22]. Although waveguide nonlinear crystals exhibit superior performances in QFT, waveguide nonlinear crystals with low insertion and transmission losses are difficult to fabricate and are severely affected by manufacturing processes. The bulk-crystal counterpart exhibits no input-light coupling-loss problems, and the technique is mature. The use of a bulk-crystal single-bit QFT for preserving polarization entanglement properties was investigated, but its external conversion efficiency was low [23]. Simultaneous QFT of a two-bit NIPEPS to generate VBPEPS has not been reported.

Here, we demonstrate a 634-nm degenerate visible-band polarization-entangled photon source based on the simultaneous polarization-independent quantum frequency transduction of two-bit 1080-nm near-infrared polarization-entangled photon source. Two polarization-independent quantum frequency transduction modules were constructed via a Sagnac-loop interferometer. The generated VBPEPS quality was characterized with standard methods, such as two-photon polarization interference, Bell inequality, and quantum state tomography. The 634-nm VBPEPS performances were also compared with those of the original 1080-nm NIPEPS, which verified that the polarization-independent quantum frequency transduction preserved the polarization entanglement. Furthermore, the phase stability and quantum efficiency of the polarization-independent quantum frequency transduction were investigated, and PIQFT had exhibited both high stability and high quantum efficiency. The external quantum efficiency include optical component loss and fiber coupling loss of our two polarization-independent quantum frequency transduction modules was 6.8% and 18.0%, respectively, which is the highest reported for a bulk crystal PIQFT. The previously reported conversion efficiency was approximately 0.04% [23]. In principle, the results here could be applied to other visible wavelengths or the ultraviolet, suggesting promising applications in quantum optical microscopy, quantum spectroscopy, and quantum networks. Thus, this work is crucial for generating polarization-entangled photon sources having different wavelengths to access various quantum systems.

II. EXPERIMENTAL METHODS

The VBPEPS experimental configuration is shown in Fig. 1. The second-harmonic generation (SHG) module is shown in Fig. 1(a), where a potassium titanyl phosphate crystal (KTP) crystal was used to generate a 40-mW 540-nm second harmonic via type-2 noncritical phase-matching. This was the pump light for the NIPEPS. The input 1080-nm pump was from a diode laser amplified via a ytterbium-doped fiber amplifier. In the second NIPEPS module shown in Fig. 1(b), the bidirectionally pumped polarization-entangled photon-source configuration of the Sagnac interferometer was used [24]. In *a*-cut KTP, the crystals satisfied the type-II noncritical phase-matching condition [25], and yielded 1080-nm degenerate photon pairs at 60 °C. From the polarization Sagnac interferometer, we obtained the following output state:

$$|\Psi\rangle \propto (|H_{s1}V_{i2}\rangle + \beta e^{i\varphi} |V_{s1}H_{i2}\rangle). \quad (1)$$

The subscripts 1 and 2 represent different output ports of the polarizing beam splitter (PBS), the subscripts *s* and *i* represent the SPDC-generated signal and idler photons, respectively; φ is the phase related to the material dispersion of the interferometer components and the pump-light polarization state; and β is related to the horizontal or vertical (*H/V*) polarization ratio of the pump light and the photon generation efficiency of the respective SPDC process. Through a series of filters, the output photon pairs were collected via an optical fiber for transmission to the QFT module to produce a PEPS in the visible wavelength band, or for coincidence measurements with silicon avalanche photodiode (APD) or indium-gallium-arsenic [(In, Ga)As] detectors (ID220-FR) to characterize the source.

The conversion device consisted of two sets of Sagnac-loop PIQFT devices [26], without additional active phase locking, to simultaneously frequency transduce the entangled photon pairs, as shown in Figs. 1(c) and 1(d). The PIQFT1 and PIQFT2 modules received photons collected by the two ports of the NIPEPS via optical fibers. The collected 1080-nm photons were combined with the strong 1540-nm pump field at the DM and then inputted into the Sagnac interferometer. The 1540-nm pump beam was from a diode laser and was amplified via another erbium-doped fiber amplifier. The *V*-polarized signal light and the pump light were mixed in the periodically poled lithium niobate crystal (PPLN) crystal to generate *V*-polarized 634.8-nm light via type-0 sum-frequency generation. The conversion light was rotated to *H* polarization via the half-wave plate (HWP). The *H*-polarized signal light and pump light were first converted to the *V*-polarized state with a HWP, after which *V*-polarized conversion light was generated in the PPLN crystal. The quantum frequency conversion efficiency was a function of the pump-light intensity, but the QFT structure of the Sagnac interferometer naturally split the input pump power into two components, thus reducing

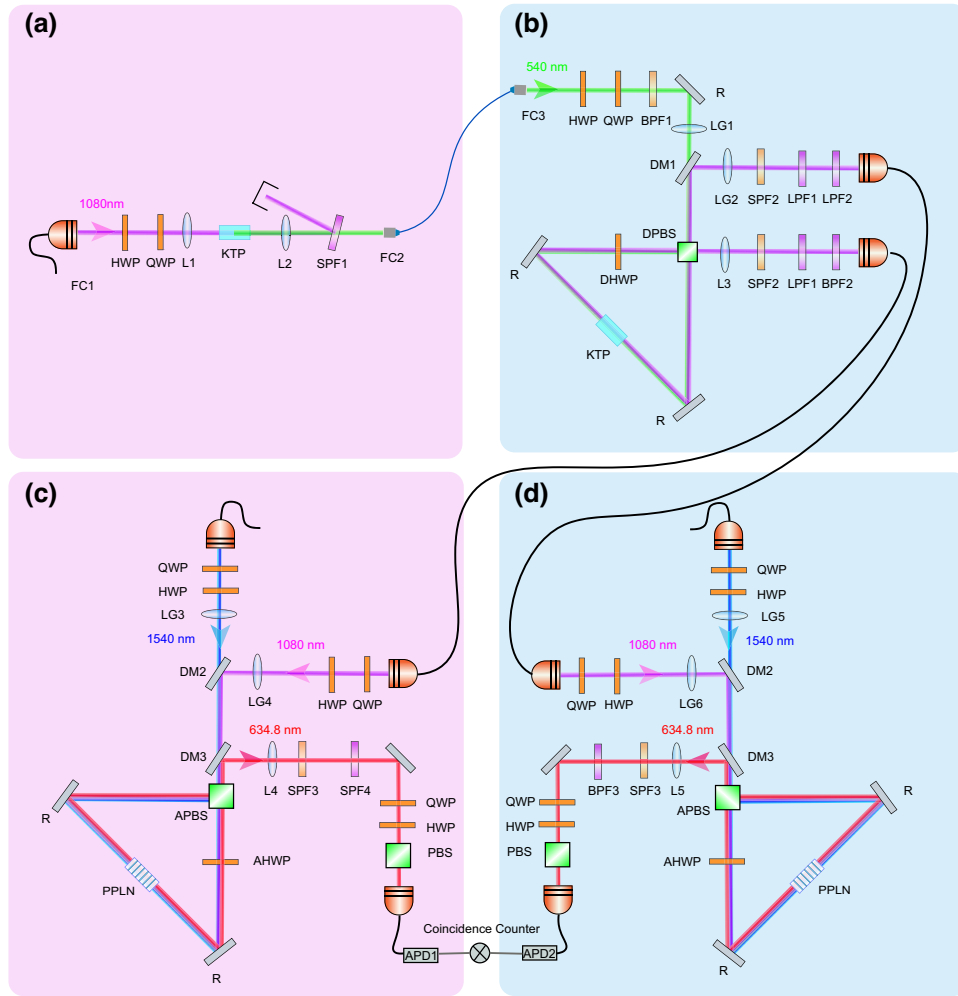


FIG. 1. (a) Second-harmonic generation (SHG) module for preparing the pump beam for the polarization-entangled photon sources (PEPSs). KTP, potassium titanyl phosphate crystal with a size of $8 \text{ mm} \times 5 \text{ mm} \times 5 \text{ mm}$ (height); HWP, half-wave plate; QWP, quarter-wave plate; SPF1, 650-nm short-pass filter. (b) Near-infrared PEPS (NIPEPS) system for preparing 1080-nm polarization-entangled photon pairs. BPF1, 520-40-nm band-pass filter; DM1, dichroic mirror; LPF1, 750-nm long-pass filter; LPF2, 600-nm long-pass filter; BPF2, 1075-50-nm band-pass filter; SPF2, 1200-nm short-pass filter; DPBS, dichroic polarizing beam splitter; LG, lens group; DHWP, dichroic wave plate. (c) Polarization-independent quantum frequency transduction1 (PIQFT1) module for entangled photon frequency transduction. DM1, 1180-nm long-pass dichroic mirror; DM2, 950-nm long-pass dichroic mirror; APBS, achromatic polarizing beam splitter; AHWP, achromatic half-wave plate; R, silver reflector; PPLN, MgO-doped periodically poled lithium niobite crystal. The period was $11.80 \mu\text{m}$. SPF3, 1200-nm short-pass filter; SPF4, 650-nm short-pass filter. LG, lens group; PBS, polarizing beam splitter; APD, silicon avalanche photodiode (Excelitas, SPCM-AQRH-14-FC). (d) PIQFT2 module. This section was configured in accordance with PIQFT1. The PPLN crystals in PIQFT1 and PIQFT2 were identical with five periodically poled gratings, where each grating was $35 \text{ mm} \times 1 \text{ mm} \times 0.5 \text{ mm}$. BPF3, 650-50-nm band-pass filter.

the conversion efficiency. To improve the efficiency, we used two different amplifiers for the generation of the pump light required for PIQFT1 and PIQFT2, which could cause problems in the relative phases between the H - and V -polarization states. We demonstrated that the relative phase of the entangled state was independent of the initial phase, frequency, and path of the pump laser between the two sets of PIQFTs, and was only affected by the polarization state of the pump light and the intrinsic material dispersion, which varied slowly with time. A detailed derivation

is given in [Appendix](#). By adjusting the pump-light HWPs and QWPs in PIQFT1 and PIQFT2, and ignoring the irrelevant total phase factor, the frequency-transformed quantum state was given by

$$|\Psi\rangle = \frac{1}{\sqrt{2}} \left(|H'_{s1}V'_{t2}\rangle + |V'_{s1}H'_{t2}\rangle \right). \quad (2)$$

The superscript $'$ denotes the 634-nm polarization-entangled state. Then, the converted light with H and V

polarizations was coherently output at the PBS and separated from the pump and signal beams by the DM. After filtering, the light was coupled into the optical fiber and detected by a silicon APD detector. We could optionally insert QWP, HWP, and PBS to perform quantum state tomography or to measure interference visibility. Finally, we obtained a 634-nm VBPEPS via pump light from two different amplifiers.

III. RESULTS AND DISCUSSION

We first describe the performance of the QFT module and results are shown in Table I. The conversion efficiencies of the PIQFT1 and PIQFT2 modules were measured as a function of pump power in the presence of the weak classical signal light. Figure 2(a) shows the net quantum efficiency (NQE) of the PIQFT1 module for H - and V -polarized input light where the optical losses are excluded and fits the NQE with $\eta = \sin^2\left(\sqrt{\pi^2 P/4P_{\max}}\right)$ [27]. The PIQFT1 optical losses for H - and V -polarized light, including the loss of the optical elements and the fiber coupling loss of converted light, were 61.87% and 58.99%, respectively. By adjusting the pump-light phase of both polarization states to balance the conversion efficiency and including the optical losses, we obtained a 6.8% external conversion efficiency in the PIQFT1 module at 108.1 °C, with a total input pump power of 7.46 W. Figure 2(b) shows the NQE performance of the PIQFT2 module. The H and V optical losses were 56.57% and 53.97%, respectively. We obtained a 18.0% external conversion efficiency at 109 °C, with a total input pump power of 10.4 W. The difference between the conversion efficiencies of the two modules were mainly attributed to the difference in focusing parameters of the Gaussian beam, and to the difference in mode matching between the signal photon and the slightly astigmatic pump beam. Because of the dispersion of the light emitted by the fiber collimation package, the pump and signal beam waists in PIQFT1 were approximately 110 and 70 μm , respectively, which were far from the calculated optimal beam waist parameters for 70.23 and 64.37 μm , respectively. The PIQFT2 pump beam was first collimated and then focused in the crystal by the lens group with a beam waist of approximately 75 μm and a signal beam waist of approximately 66

TABLE I. The performance of the PIQFT modules.

Type	PIQFT module 1	PIQFT module 2
H -arm optical loss	61.87%	56.57%
V -arm optical loss	58.99%	53.97%
PIQFT module external conversion efficiency	6.8%	18.0%
Pump beam waist	110 μm	75 μm
Signal beam waist	70 μm	66 μm

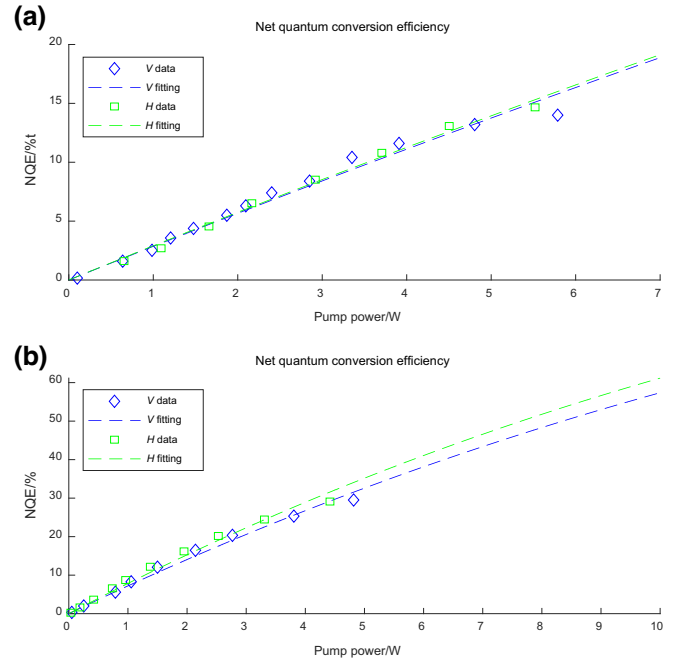


FIG. 2. (a) PIQFT1 net quantum efficiency. Vertical (V) polarization data are blue diamonds and horizontal (H) polarization data are green squares. The corresponding fitted curves are dashed lines with corresponding colors. (b) PIQFT2 net quantum efficiency.

μm , resulting in a high conversion efficiency. The average single-photon external conversion efficiency was 11.06%, which is the average of two PIQFT conversion efficiencies, and the external conversion efficiency for the photon pairs was 1.22%, which is the product of two PIQFT conversion efficiencies. We obtained the observed brightness of 1080-nm NIPEPS and 634-nm VBPEPS as 1.3 and 0.4 pairs/s/mW with 30-mW 540-nm pump power, respectively, from direct measurements with silicon APD detectors. The generated intrinsic brightness after correction for losses, detection efficiencies, and collection efficiencies in the setup for NIPEPS and VBPEPS were 123 076 and 31 645 pairs/s/mW, respectively. According to our previous work, the photonic bandwidths of NIPEPS and VBPEPS are about 2.4 and 0.4 nm, respectively [28]. The difference in brightness is due to the filtering effect introduced by the QFT, where the 0.265-nm acceptance bandwidth was smaller than the 2.8-nm photon bandwidth of the photon pairs generated by the SPDC. The dark count rates for the PIQFT1 and PIQFT2 modules were measured to be 2000 ± 300 and 1500 ± 400 Hz, respectively, without entangled photons as input. The accidental coincidence rate was 9 Hz for VBPEPS with 30-s integration times and 3 Hz for NIPEPS with 10-s integration times. The coincidence signal-to-background ratios before and after conversion were 98.5 and 36.9, respectively.

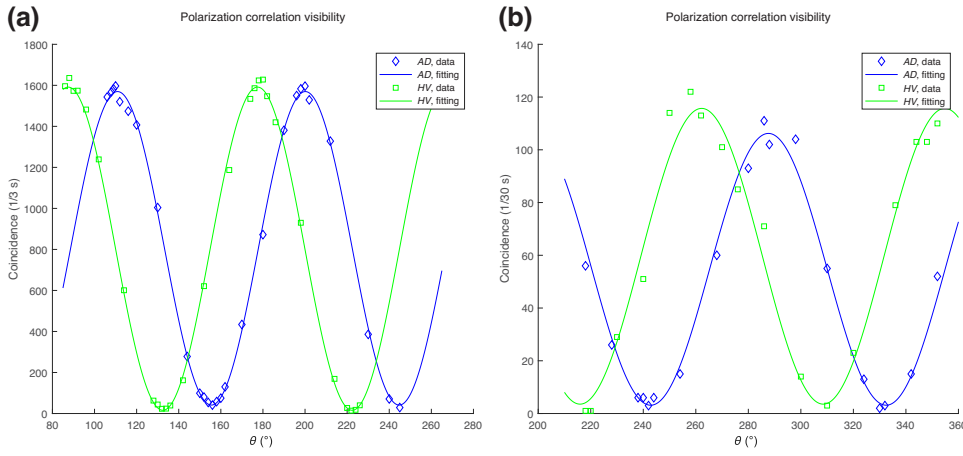


FIG. 3. Two-photon coincidences as a function of the half-wave plate angle of the polarization projection measurement module. The blue diamonds and green squares are coincidence count data for fixing the other measuring arms to $|H\rangle$ and $|D\rangle$, respectively. The sinusoidal fits are the blue and green solid lines, respectively. (a) Measurement of the NIPEPS. (b) Measurement of the VBPEPS.

It was important to verify preservation of the polarization entanglement property before and after the PIQFT. Violation of the Bell inequality was an effective method for strictly determining the presence of entanglement. We measured the CHSH inequality [29], constructed with the S parameter:

$$S = |E(a, b) - E(c, d)| + |E(d, c) + E(d, b)| \leq 2. \quad (3)$$

We set the angle to $a = 0, b = (\pi/8), c = (3\pi/8), d = (\pi/4)$. The classical limit of an S value above 2 indicates

a measured state that is incompatible with the local model of reality and that entanglement exists. We measured the coincidence counts of 16 sets of bases, including the above angle with rotation $\pi/2$, to obtain the S parameters because the experimental configuration enabled us to obtain data for only one set of measurement bases in a single measurement. We measured the S -parameters of the entangled photon source before conversion using (In, Ga)As detectors with 30-s integration times: $S_{1080} = 2.710 \pm 0.034$. Similarly, the parameters of the converted entangled photon source S were $S_{634} = 2.619 \pm 0.046$ with

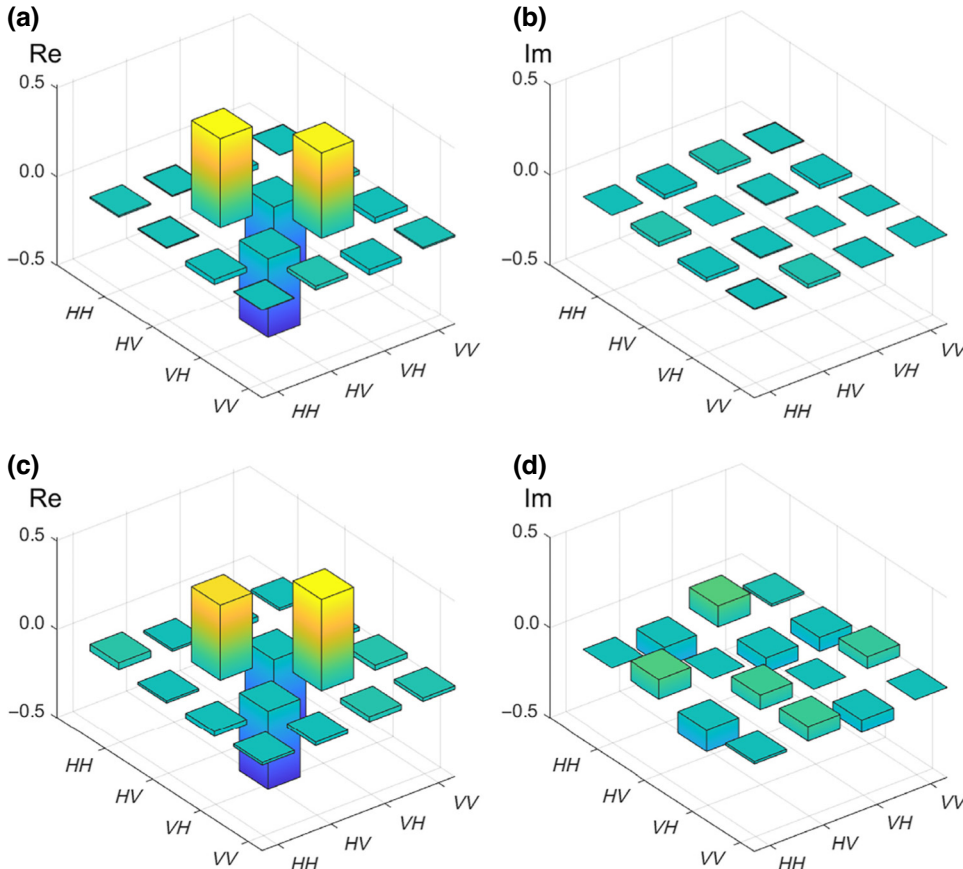


FIG. 4. Reconstructed density matrix for polarization-entangled photon pairs at 1080 and 634 nm. (a) Real parts of the unconverted-state density matrix. (b) Imaginary parts of the unconverted-state density matrix. (c) Real parts of the converted-state density matrix. (d) Imaginary parts of the converted-state density matrix.

TABLE II. Comparison of different polarization-entangled photon sources.

Ref.	Type	Wavelength (nm)	Bandwidth	Brightness
This work	PIQFT SPDC	634	110 GHz (0.4 nm)	79 k pairs/s/mW/nm
[12]	directly SPDC	532	25 THz (24 nm)	14 k pairs/s/mW/nm ^a
[32]	atoms SFWM	780 ^b	6 MHz	320 pairs/s ^c

^aThe spectral brightness here is obtained from 9.5 k pairs/s/mW after correcting the 16.7% average heralding.

^bHere nondegenerate photon pairs are generated near 780 with a spacing of $2\pi \times 86$ MHz.

^cBrightness takes into account transmission losses and duty cycle.

silicon APD detectors. It still maintained excellent entanglement properties.

We measured the polarization correlation visibility of the unconverted entangled photon sources [30]. Figure 3(a) shows the coincidence counts as a function of the signal photon HWP angle θ_1 when the idler photon was projected on to $|H\rangle, |D\rangle$. We obtained higher coincidence counts using an (In, Ga)As detector that had a higher detection efficiency than that of the silicon APD at 1080 nm, and the visibility was $V_{HV} = 98.08\%$ in the H - V base and $V_{AD} = 94.88\%$ in the A - D base under the best fit. As shown in Fig. 3(b), we also measured the polarization correlation visibility of the converted entangled photon source. The visibility was $V'_{HV} = 94.01\%$ in the H - V base and $V'_{AD} = 94.24\%$ in the A - D base with silicon APD detectors. The experimental setup of two sets of Sagnac interferometer structures introduced in the QFT process led to a slight decrease in interference visibility, which demonstrated the superior performance of our PIQFT system

To further clarify the quantum states before and after the conversion of the entangled photon source, we performed two-qubit quantum state tomography [31] to characterize the 1080- and 634-nm quantum states, respectively. We measured the coincidence counts under 16 measurement criteria based on $\{|H\rangle, |V\rangle, |R\rangle, \text{ and } |D\rangle\}$ for the unconverted entangled photon source in the (In, Ga)As detector configuration for 3 s, and reconstructed the two-bit polarization-entangled state from the measurement data using maximum-likelihood optimization. The results are shown in Figs. 4(a) and 4(b). Additionally, for the converted 634-nm entangled photon source, we measured using the silicon APD detector configuration for 30 s and reconstructed the results, as shown in Figs. 4(c) and 4(d). From the reconstructed results, we calculated the fidelity of the quantum state (with Bell state ϕ^-), the fidelity before the conversion $F_{1080} = 94.08 \pm 0.83\%$, and the fidelity after the conversion $F_{634} = 92.93 \pm 2.38\%$. The error was determined assuming Poisson count statistics. The decrease in the fidelity of the entangled photon source after conversion was mainly attributed to the mismatch between the conversion efficiencies of the H and V polarizations in the PIQFT setup and the relative phase, which was not perfectly tuned to π . The transduction fidelity was $F_{\text{QFT}} = (F_{634}/F_{1080}) = 98.78\%$. Eventually,

we obtained VBPEPS with high fidelity using the PIQFT technique.

In Table II, we compared the performance of our source with that of other works on the visible band. The result shows that the excellent brightness performance of our source. With the optimization of the NIPEPS source, we can further obtain narrower bandwidth, higher brightness, and fidelity VBPEPS. In particular, our technology has the potential to yield high-performance UV sources. Considering the coupling to the N- V color center system at 637 nm with a zero-phonon emission linewidth of about 1 GHz, a narrow-band filtering of our system results in a decrease in brightness of about 300 pairs/s/mW. This is still consistent with the brightness of the source generated directly by the atomic system. Although atomic, etc., systems can directly generate narrow bandwidth photon sources, their wavelengths are limited by atomic energy levels and cannot be arbitrarily tuned. And its absolute photon generation rate is low, which cannot be applied to quantum imaging and other fields that require high brightness.

IV. CONCLUSIONS

In conclusion, we used the PIQFT technique to convert a NIPEPS to visible wavelengths with 98.78% transduction fidelity. We obtained a visible-band polarization-entangled photon source with 31645 pairs/s/mW brightness at 11% average single photon conversion efficiency. The fidelity and Bell S parameter measured for the VBPEPS were 92.9% and 2.619, respectively, which indicated that our VBPEPS had high entanglement quality.

We could improve the external conversion efficiency by further optimization of the Gaussian-beam focusing parameters in the QFT module. The utilization of higher transmittance optical components would also be a potential approach. The self-phase stability of the PIQFT was verified by using different amplifier pumps, which indicated that different pump sources could be used instead of a single high-power source to obtain a higher conversion efficiency. This finding also indicated that we could use different pump sources for different nonlinear processes. For example, we could obtain 637-nm degenerate polarized entangled photon pairs, which correspond to N- V

center excitation spectra. [33], by tuning the pump wavelengths of two PIQFTs to 1553 nm at 150 °C; these pairs also play a role in N-*V* center storage [34,35].

VBPEPSs have pivotal applications in quantum microscopy and imaging [36–39] because they work in at the efficient-detection wavelengths of silicon single-photon avalanche diodes, and are nondestructive to sensitive biological samples, including live cells and organisms. Furthermore, the method could involve a quantum state frequency interface [40,41]. The filtering effect of the up-conversion process enabled us to obtain narrow-band visible photons, allowing access to quantum systems such as ions and solids [42]. Through the inverse process, we could access the C-band communication system, which has been used for long-range quantum state distributions [43].

ACKNOWLEDGMENTS

We would like to acknowledge the support from the National Key Research and Development Program of China (Grants No. 2022YFB3607700, No. 2022YFB3903102), National Natural Science Foundation of China (NSFC) (Grants No. 11934013, No. 92065101, No. 62005068), and Innovation Program for Quantum Science and Technology (Grant No. 2021ZD0301100), and the Space Debris Research Project of China (Grant No. KJSP2020020202).

The authors declare no conflicts of interest.

APPENDIX: PHASE STABILITY OF THE DUAL-PUMP SAGNAC QFT

Phase self-stabilization of a polarization-entangled photon source with a Sagnac-loop structure has been demonstrated [44]. Here, we extended this to sum-frequency processes and considered the effect of dual-pump lasers. We set L_A to represent the path length from the polarization beam splitter (PBS) to the center of the crystal in the clockwise direction, and L_B to the center of the crystal in the counterclockwise direction. L represents the distance that the pump light passes before entering the interferometer. The pump light input field is given by

$$E_p = (E_H \hat{e}_H + e^{i\varphi_p} E_V \hat{e}_V) e^{i(k_p L + \varphi_{p_0})}. \quad (\text{A1})$$

φ_p represents the phase difference between the orthogonal polarization states of the pump light, φ_{p_0} represents the intrinsic phase factor determined by the pump laser itself, and k_p represents the 1540-nm pump-light wave vector. \hat{e}_H and \hat{e}_V are the horizontal *H* and vertical *V* polarization unit vectors, respectively. Considering that the phase of the conversion light for the sum-frequency process is determined by the pump light and the signal light, the phase of the *H*-polarized state conversion light after one rotation

around the loop is given by

$$\varphi_{\text{conH}} = L_A k_p + L_A k_s + L_B k_c + \varphi_{\text{dispH}}. \quad (\text{A2})$$

Similarly, for *V*-polarized conversion light, the phase is given by

$$\varphi_{\text{conV}} = L_B k_p + L_B k_s + L_A k_c + \varphi_{\text{dispV}}. \quad (\text{A3})$$

$\varphi_{\text{dispH/V}}$ is the extra phase attributed to the *H/V* polarized light passing through the optical components. k_s is the wave vector of the 1080-nm signal light, and k_c is the wave vector of the converted 634-nm conversion light. For the input quantum state from the NIPEPS $|H_s V_i\rangle + |V_s H_i\rangle$, considering the phase of the pump light outside the Sagnac loop, the converted quantum state is given by

$$|\Psi\rangle \propto \left(e^{i\varphi_{\text{conH}}} |H'_s V'_i\rangle + \beta e^{i(\varphi_{\text{conV}} + \varphi_p)} |V'_s H'_i\rangle \right) e^{i(k_p L + \varphi_{p_0})} \quad (\text{A4})$$

$$\beta = \frac{\eta_H E_H}{\eta_V E_V}, \quad (\text{A5})$$

where $\eta_{H/V}$ is the *H/V* polarization light conversion efficiency in the Sagnac loop, and the superscript ' represents the converted photon. In free space,

$$k_p + k_s = k_c. \quad (\text{A6})$$

Thus, the converted quantum state can be given by

$$|\Psi\rangle \propto \left(|H'_s V'_i\rangle + e^{i(\varphi_{\text{disp}} + \varphi_p)} \beta |V'_s H'_i\rangle \right) e^{i(k_p L + \varphi_{p_0} + (L_A + L_B)k_c)}. \quad (\text{A7})$$

Similarly, the input H_i, V_i photons are converted by a pump beam from another amplifier. The superscripts 1 and 2 distinguish the loops PIQFT1 and PIQFT2, respectively. Then, the quantum state of the entangled source photon after the QFT can be given by

$$|\Psi\rangle \propto \left(|H'_s V'_i\rangle + e^{i(\varphi_{\text{disp}}^1 + \varphi_{\text{disp}}^2 + \varphi_p^1 + \varphi_p^2)} \beta^1 \beta^2 |V'_s H'_i\rangle \right) \times e^{i(k_p L^1 + k_p L^2 + \varphi_{p_0}^1 + \varphi_{p_0}^2 + (L_A^1 + L_B^1 + L_A^2 + L_B^2)k_c)}. \quad (\text{A8})$$

The above equation illustrates that the phase of the entangled state is independent of the initial phase, frequency, and path of the pump laser between the two sets of PIQFTs, and is affected only by the pump light phase and the intrinsic material dispersion, which varies slowly with time. We set $\varphi_{\text{disp}}^1 + \varphi_{\text{disp}}^2 + \varphi_p^1 + \varphi_p^2 = 0$, $\beta^1 \beta^2 = 1$ by adjusting the pump-light HWPs and QWPs in PIQFT1 and

PIQFT2, ignoring the irrelevant total phase factor. The frequency-transformed quantum state is thus given by

$$|\Psi\rangle \propto \left|H'_{s1}V'_{i2}\right\rangle + \left|V'_{s1}H'_{i2}\right\rangle. \quad (\text{A9})$$

This shows that, in principle, the use of different amplifiers to generate the pump light does not affect the coherence of the entangled photon source during the QFT.

-
- [1] H. J. Kimble, The quantum internet, *Nature* **453**, 1023 (2008).
- [2] L. Jiang, J. M. Taylor, A. S. Sørensen, and M. D. Lukin, Distributed quantum computation based on small quantum registers, *Phys. Rev. A* **76**, 062323 (2007).
- [3] N. Kalb, A. A. Reiserer, P. C. Humphreys, J. J. W. Bakermans, S. J. Kamerling, N. H. Nickerson, S. C. Benjamin, D. J. Twitchen, M. Markham, and R. Hanson, Entanglement distillation between solid-state quantum network nodes, *Science* **356**, 928 (2017).
- [4] J. Hannegan, J. D. Siverns, and Q. Quraishi, Entanglement between a trapped-ion qubit and a 780-nm photon via quantum frequency conversion, *Phys. Rev. A* **106**, 042441 (2022).
- [5] A. Kuzmich, W. P. Bowen, A. D. Boozer, A. Boca, C. W. Chou, L.-M. Duan, and H. J. Kimble, Generation of non-classical photon pairs for scalable quantum communication with atomic ensembles, *Nature* **423**, 731 (2003).
- [6] L. Childress and R. Hanson, Diamond NV centers for quantum computing and quantum networks, *MRS Bull.* **38**, 134 (2013).
- [7] P. G. Kwiat, K. Mattle, H. Weinfurter, A. Zeilinger, A. V. Sergienko, and Y. Shih, New high-intensity source of polarization-entangled photon pairs, *Phys. Rev. Lett.* **75**, 4337 (1995).
- [8] X. Li, P. L. Voss, J. E. Sharping, and P. Kumar, Optical-fiber source of polarization-entangled photons in the 1550 nm telecom band, *Phys. Rev. Lett.* **94**, 053601 (2005).
- [9] Y.-H. Li, Z.-Y. Zhou, Z.-H. Xu, L.-X. Xu, B.-S. Shi, and G.-C. Guo, Multiplexed entangled photon-pair sources for all-fiber quantum networks, *Phys. Rev. A* **94**, 043810 (2016).
- [10] M. Ren *et al.*, Roadmap on nonlinear optics-focus on Chinese research, *J. Phys.: Photonics* **5**, 032501 (2023).
- [11] Y. Li, Z.-Y. Zhou, D.-S. Ding, and B.-S. Shi, CW-pumped telecom band polarization entangled photon pair generation in a Sagnac interferometer, *Opt. Express* **23**, 28792 (2015).
- [12] A. Sansa Perna, E. Ortega, M. Gräfe, and F. Steinlechner, Visible-wavelength polarization-entangled photon source for quantum communication and imaging, *Appl. Phys. Lett.* **120**, 074001 (2022).
- [13] A. Fedrizzi, T. Herbst, A. Poppe, T. Jennewein, and A. Zeilinger, A wavelength-tunable fiber-coupled source of narrowband entangled photons, *Opt. Express* **15**, 15377 (2007).
- [14] Y. H. Xin Wen and J. Wang, Comparison and characterization of efficient frequency doubling at 397.5 nm with PPKTP, LBO and BIBO crystals, *Laser Phys.* **26**, 045401 (2016).
- [15] D. Borodin, S. Levy, and S. Shwartz, High energy-resolution measurements of x -ray into ultraviolet parametric down-conversion with an x -ray tube source, *Appl. Phys. Lett.* **110**, 131101 (2017).
- [16] W. Wieczorek, R. Krischek, A. Ozawa, G. Tóth, N. Kiesel, P. Michelberger, T. Udem, and H. Weinfurter, in *Quantum Optics*, Vol. 7727, edited by V. N. Zadkov and T. Durt, International Society for Optics and Photonics (SPIE, 2010) p. 77270L.
- [17] S. Tanzilli, W. Tittel, M. Halder, O. Alibart, P. Baldi, N. Gisin, and H. Zbinden, A photonic quantum information interface, *Nature* **437**, 116 (2005).
- [18] H. Takesue, E. Diamanti, C. Langrock, M. M. Fejer, and Y. Yamamoto, 1.5- μm single photon counting using polarization-independent up-conversion detector, *Opt. Express* **14**, 13067 (2006).
- [19] F. Kaiser, P. Vergyris, A. Martin, D. Aktas, M. P. D. Micheli, O. Alibart, and S. Tanzilli, Quantum optical frequency up-conversion for polarisation entangled qubits: Towards interconnected quantum information devices, *Opt. Express* **27**, 25603 (2019).
- [20] M. A. Albota, F. N. C. Wong, and J. H. Shapiro, Polarization-independent frequency conversion for quantum optical communication, *J. Opt. Soc. Am. B* **23**, 918 (2006).
- [21] E. Arenskötter, T. Bauer, S. Kucera, M. Bock, J. Eschner, and C. Becher, Telecom quantum photonic interface for a $^{40}\text{Ca}^+$ single-ion, *npj Quantum Inf.* **9**, 34 (2023).
- [22] T. van Leent, M. Bock, F. Fertig, R. Garthoff, S. Eppelt, Y. Zhou, P. Malik, M. Seubert, T. Bauer, W. Rosenfeld, W. Zhang, C. Becher, and H. Weinfurter, Entangling single atoms over 33 km telecom fibre, *Nature* **607**, 69 (2022).
- [23] S. Ramelow, A. Fedrizzi, A. Poppe, N. K. Langford, and A. Zeilinger, Polarization-entanglement-conserving frequency conversion of photons, *Phys. Rev. A* **85**, 013845 (2012).
- [24] B.-S. Shi and A. Tomita, Generation of a pulsed polarization entangled photon pair using a Sagnac interferometer, *Phys. Rev. A* **69**, 013803 (2004).
- [25] Z. Y. Ou, S. F. Pereira, E. S. Polzik, and H. J. Kimble, 85% efficiency for CW frequency doubling from 1.08 to 0.54 μm , *Opt. Lett.* **17**, 640 (1992).
- [26] R. Ikuta, T. Kobayashi, T. Kawakami, S. Miki, M. Yabuno, T. Yamashita, H. Terai, M. Koashi, T. Mukai, T. Yamamoto, and N. Imoto, Polarization insensitive frequency conversion for an atom-photon entanglement distribution via a telecom network, *Nat. Commun.* **9**, 1997 (2018).
- [27] M. A. Albota and F. N. C. Wong, Efficient single-photon counting at 1.55 μm by means of frequency upconversion, *Opt. Lett.* **29**, 1449 (2004).
- [28] C. Yang, S.-J. Niu, Z.-Y. Zhou, Y. Li, Y.-H. Li, Z. Ge, M.-Y. Gao, Z.-Q.-Z. Han, R.-H. Chen, G.-C. Guo, and B.-S. Shi, Advantages of the frequency-conversion technique in quantum interference, *Phys. Rev. A* **105**, 063715 (2022).
- [29] J. F. Clauser, M. A. Horne, A. Shimony, and R. A. Holt, Proposed experiment to test local hidden-variable theories, *Phys. Rev. Lett.* **23**, 880 (1969).
- [30] A. Anwar, C. Perumangatt, F. Steinlechner, T. Jennewein, and A. Ling, Entangled photon-pair sources based on three-wave mixing in bulk crystals, *Rev. Sci. Instrum.* **92**, 041101 (2021).

- [31] D. F. V. James, P. G. Kwiat, W. J. Munro, and A. G. White, Measurement of qubits, *Phys. Rev. A* **64**, 052312 (2001).
- [32] H. Yan, S. Zhang, J. F. Chen, M. M. T. Loy, G. K. L. Wong, and S. Du, Generation of narrow-band hyperentangled non-degenerate paired photons, *Phys. Rev. Lett.* **106**, 033601 (2011).
- [33] M. W. Doherty, N. B. Manson, P. Delaney, F. Jelezko, J. Wrachtrup, and L. C. Hollenberg, The nitrogen-vacancy colour centre in diamond, *Phys. Rep.* **528**, 1 (2013).
- [34] E. Togan, Y. Chu, A. S. Trifonov, L. Jiang, J. Maze, L. Childress, M. V. G. Dutt, A. S. Sørensen, P. R. Hemmer, A. S. Zibrov, and M. D. Lukin, Quantum entanglement between an optical photon and a solid-state spin qubit, *Nature* **466**, 730 (2010).
- [35] H. Bernien, B. Hensen, W. Pfaff, G. Koolstra, M. S. Blok, L. Robledo, T. H. Taminiau, M. Markham, D. J. Twitchen, L. Childress, and R. Hanson, Heralded entanglement between solid-state qubits separated by three metres, *Nature* **497**, 86 (2013).
- [36] B. Ndagano, H. Defienne, D. Branford, Y. D. Shah, A. Lyons, N. Westerberg, E. M. Gauger, and D. Faccio, Quantum microscopy based on Hong–Ou–Mandel interference, *Nat. Photonics* **16**, 384 (2022).
- [37] J. Liu, Q. Yang, S. Chen, Z. Xiao, S. Wen, and H. Luo, Intrinsic optical spatial differentiation enabled quantum dark-field microscopy, *Phys. Rev. Lett.* **128**, 193601 (2022).
- [38] P.-A. Moreau, E. Toninelli, T. Gregory, and M. J. Padgett, Imaging with quantum states of light, *Nat. Rev. Phys.* **1**, 367 (2019).
- [39] C. A. Casacio, L. S. Madsen, A. Terrasson, M. Waleed, K. Barnscheidt, B. Hage, M. A. Taylor, and W. P. Bowen, Quantum-enhanced nonlinear microscopy, *Nature* **594**, 201 (2021).
- [40] M. Bock, P. Eich, S. Kucera, M. Kreis, A. Lenhard, C. Becher, and J. Eschner, High-fidelity entanglement between a trapped ion and a telecom photon via quantum frequency conversion, *Nat. Commun.* **9**, 1998 (2018).
- [41] M. Ruf, N. H. Wan, H. Choi, D. Englund, and R. Hanson, Quantum networks based on color centers in diamond, *J. Appl. Phys.* **130**, 070901 (2021).
- [42] T. P. Harty, D. T. C. Allcock, C. J. Ballance, L. Guidoni, H. A. Janacek, N. M. Linke, D. N. Stacey, and D. M. Lucas, High-fidelity preparation, gates, memory, and readout of a trapped-ion quantum bit, *Phys. Rev. Lett.* **113**, 220501 (2014).
- [43] T. van Leent, M. Bock, R. Garthoff, K. Redeker, W. Zhang, T. Bauer, W. Rosenfeld, C. Becher, and H. Weinfurter, Long-distance distribution of atom-photon entanglement at telecom wavelength, *Phys. Rev. Lett.* **124**, 010510 (2020).
- [44] T. Kim, M. Fiorentino, and F. N. C. Wong, Phase-stable source of polarization-entangled photons using a polarization Sagnac interferometer, *Phys. Rev. A* **73**, 012316 (2006).